Opto-Electronic
Science

ISSN 2097-0382 CN 51-1800/O4

31.38 Gb/s GaN-based LED array visible light communication system enhanced with V-pit and sidewall quantum well structure

Zengyi Xu, Wenqing Niu, Yu Liu, Xianhao Lin, Jifan Cai, Jianyang Shi, Xiaolan Wang, Guangxu Wang, Jianli Zhang, Fengyi Jiang, Zhixue He, Shaohua Yu, Chao Shen, Junwen Zhang and Nan Chi

Citation: Xu ZY, Niu WQ, Liu Y, Lin XH, Cai JF et al. 31.38 Gb/s GaN-based LED array visible light communication system enhanced with V-pit and sidewall quantum well structure. *Opto-Electron Sci* **2**, 230005 (2023).

https://doi.org/10.29026/oes.2023.230005

Received: 5 April 2023; Accepted: 16 July 2023; Published online: 28 July 2023

Related articles

Demonstration of a low-complexity memory-polynomial-aided neural network equalizer for CAP visible-light communication with superluminescent diode

Fangchen Hu, Jorge A. Holguin-Lerma, Yuan Mao, Peng Zou, Chao Shen, Tien Khee Ng, Boon S. Ooi, Nan Chi

Opto-Electronic Advances 2020 **3**, 200009 doi: 10.29026/oea.2020.200009

High-speed visible light communication based on micro-LED: A technology with wide applications in next generation communication

Tingwei Lu, Xiangshu Lin, Wenan Guo, Chang-Ching Tu, Shibiao Liu, Chun-Jung Lin, Zhong Chen, Hao-Chung Kuo, Tingzhu Wu

Opto-Electronic Science 2022 **1**, 220020 doi: 10.29026/oes.2022.220020

An optimized light source layout model for visible light communication system

Liu Hong, Zhai Changxin, Wen Yanyan, Xi Lei, Du Zongyu

Opto-Electronic Engineering 2020 **47**, 190565 doi: 10.12086/oee.2020.190565

http://www.oejournal.org/oes

Website

Opto-Electronic Science

Article
May 2023, Vol. 2, No. 5

DOI: 10.29026/oes.2023.230005

31.38 Gb/s GaN-based LED array visible light communication system enhanced with V-pit and sidewall quantum well structure

Zengyi Xu[1,4], Wenqing Niu[1], Yu Liu[2], Xianhao Lin[1], Jifan Cai[1], Jianyang Shi[1,3], Xiaolan Wang[2], Guangxu Wang[2], Jianli Zhang[2], Fengyi Jiang[2], Zhixue He[4], Shaohua Yu[4], Chao Shen[1], Junwen Zhang[1] and Nan Chi[1,3]*

Although the 5G wireless network has made significant advances, it is not enough to accommodate the rapidly rising requirement for broader bandwidth in post-5G and 6G eras. As a result, emerging technologies in higher frequencies including visible light communication (VLC), are becoming a hot topic. In particular, LED-based VLC is foreseen as a key enabler for achieving data rates at the Tb/s level in indoor scenarios using multi-color LED arrays with wavelength division multiplexing (WDM) technology. This paper proposes an optimized multi-color LED array chip for high-speed VLC systems. Its long-wavelength GaN-based LED units are remarkably enhanced by V-pit structure in their efficiency, especially in the "yellow gap" region, and it achieves significant improvement in data rate compared with earlier research. This work investigates the V-pit structure and tries to provide insight by introducing a new equivalent circuit model, which provides an explanation of the simulation and experiment results. In the final test using a laboratory communication system, the data rates of eight channels from short to long wavelength are 3.91 Gb/s, 3.77 Gb/s, 3.67 Gb/s, 4.40 Gb/s, 3.78 Gb/s, 3.18 Gb/s, 4.31 Gb/s, and 4.35 Gb/s (31.38 Gb/s in total), with advanced digital signal processing (DSP) techniques including digital equalization technique and bit-power loading discrete multitone (DMT) modulation format.

Keywords: GaN-based LED; LED array; VLC; V-pit; sidewall quantum well; high-frequency response

Xu ZY, Niu WQ, Liu Y, Lin XH, Cai JF et al. 31.38 Gb/s GaN-based LED array visible light communication system enhanced with V-pit and sidewall quantum well structure. *Opto-Electron Sci* **2**, 230005 (2023).

Introduction

Around 2030, the next generation of mobile communication technology (6G) is predicted to emerge[1,2]. In 2019, the 6G white paper summarized the envision in three keywords: "Ubiquitous", "Wireless", and "Intelligence", predicting that it would provide services for users everywhere seamlessly, using critical wireless infrastructure, and in a "context-aware" manner[1]. Applications such as AR/VR, Internet of Everything (IoE), remote healthcare, industry 4.0, etc. However, the rapid growth of

[1]Key Laboratory for the Information Science of Electromagnetic Waves (MoE), Department of Communication Science and Engineering, Fudan University, Shanghai 200433, China; [2]National Institute of LED on Silicon Substrate, Nanchang University, Nanchang 330096, China; [3]Shanghai Engineering Research Center of Low-Earth-Orbit Satellite Communication and Applications, and Shanghai Collaborative Innovation Center of Low-Earth-Orbit Satellite Communication Technology, Shanghai 200433, China; [4]Peng Cheng Laboratory, Shenzhen 518055, China.
*Correspondence: N Chi, E-mail: nanchi@fudan.edu.cn
Received: 5 April 2023; Accepted: 16 July 2023; Published online: 28 July 2023

Open Access This article is licensed under a Creative Commons Attribution 4.0 International License.
To view a copy of this license, visit http://creativecommons.org/licenses/by/4.0/.

© The Author(s) 2023. Published by Institute of Optics and Electronics, Chinese Academy of Sciences.

data-hungry applications and automated systems would create an enormous data rate on terabit level, sub-millisecond latency, and massive connection in 10^7 per km^2, which is already beyond the reach of 5G millimeter-wave RF technology[3]. The usable spectrum resource with RF spectrum also become scarce and could not support the explosively growing channel capacity.

Given the highly depleted spectrum, the industry and academia are pushing communication to higher frequencies above the conventional RF range, such as THz (100 GHz-10 THz), infrared (IR), and visible light (400–800 THz). Among them, visible light communication (VLC) gains much attention from researchers due to its unique advantages such as large channel capacity, unlicensed spectrum, higher bio-safety, larger transmission in water, and intrinsic compatibility to illumination systems[4]. Multi-color LED could also form large-scale arrays to provide large capacity and serve as an important supplement to the existing technology[5]. Wavelength division multiplexing (WDM) technology can expand the channel capacity further for multi-color LED[6,7]. Recent studies on LED/micro-LED-based VLC systems are listed in Table 1. Future high-speed VLC systems may also utilise superluminescent diodes (SLDs) for over Gb/s data rate[8], however, recent research on the SLD-based VLC system is limited. Therefore, the VLC system is predicted to be a promising technique in future 6G communication, such as indoor communication, underwater networks, terrestrial network (car networks), and other areas[4].

However, there are a few hurdles for the current LED-based VLC system, for instance, the droop effect, and high-frequency loss in its most frequently used modulation scheme: intensity modulation and direct detection (IM/DD). The former prevents the growth of optical output power, and the latter not only restricts the usable bandwidth but also requires effective equalization technology that flattens the received spectrum at the cost of the received signal power, which further limits the usable signal power. Therefore, the improvement to the LED device usually focuses on either larger signal power or higher modulation bandwidth, or both.

As one viable solution, micro-LED reduces the LED chip size to improve the intrinsic modulation bandwidth. Existing research has demonstrated GHz-level modulation bandwidths[9–13] implemented by smaller device dimensions and reduced carrier lifetime. However, the high current density in micro-LED devices (usually over 1 kA/cm^2) makes it challenging to manage thermal issues and their optical power hindered long-range transmission. In contrast, while LED devices typically suffer from a less favorable electrical-optical (EO) bandwidth (usually lower than 100 MHz), their current density is orders of magnitude lower than that of micro-LEDs, which easily enables optical power over 100 mW. This advantage allows trading received power for larger signal bandwidth by applying equalization techniques and hence LED could achieve a higher data rate. The research in Table 1 shows that the modulation bandwidth applied in LED-based VLC systems also approaches the GHz level, and their data rates are at the same level

Table 1 | Performance comparison of the recent LED/micro-LED-based VLC systems.

Year	LED/Micro-LED type	Modulation bandwidth	Modulation format	Optical power (mW)	Maximum data rate (Gb/s)
2020[11]	Blue C-plane InGaN micro-LED	1.3 GHz	QPSK-OFDM	0.82	4
2021[7]	Multi-color 3 LEDs and 5 micro-LEDs	1 GHz (maximum)	Bit-power loading OFDM	4.342 (LED) 2.285 (micro-LED)	25.2
2021[12]	Blue micro-LED	1.025 GHz	QPSK-OFDM	0.9	8.75
2021[9]	Green 2x3 InGaN/GaN micro-LED Type	1.102 GHz	Bit-power loading OFDM	2.2	4.343
2022[10]	Blue C-plane InGaN/GaN	1.53 GHz	OFDM	1.5	5.27
2022[20]	2x4 Golden light LED	675 MHz	CAP	~50	5.4
2022[21]	C-plane green micro-LEDs	1.31 GHz	OFDM	2.87	5.789
2022[22]	InGaN quantum dot green micro-LED	1.22 GHz	OOK	0.18	2.1
2022[23]	Semipolar (20-21) GaN blue micro-LED	1.0425 GHz	OFDM	0.677	2.805
2016[24]	Blue micro-LED	~830 MHz	OOK	5.5	5
2023[15]	8-wavelength LED array	675 MHz (maximum)	Bit-power loading APSK DMT	~850	28.93
This work	8-wavelength LED array	800 MHz (maximum)	Bit-power loading QAM DMT	~930	31.38

compared with their micro-LED counterparts. Therefore, another approach is increasing the radiative recombination rate, reducing the droop effect and carrier lifetime, to obtain a more efficient LED device, but leaving the device size unchanged.

In this paper, the proposed device is featured in its V-pit structure (“V” shaped pits on the active layer). It is an innovative solution to the mismatch between GaN and InN lattices when Indium composition is required for longer wavelength emission. Existing papers have shown the capability of V-pit GaN-based LED array devices in communication[14,15], which results in 24 Gb/s and 28.9 Gb/s communication rates, respectively. Hu[14] used green 520 nm LED units to achieve a 2.8 Gb/s communication rate and Niu[15] obtained 3.83 Gb/s using an optimized device and the same wavelength. But the data rate still has room for improvement and it needs further investigation to associate its physical level innovation with its communication performance for future work to optimize its communication capability.

The following part of this paper first introduces the function of the V-pit structure in GaN-based LED, including its earlier research on its influence on carrier dynamics. This article tries to give an explanation based on physical level analysis and a dedicated equivalent circuit for V-pit device, which is developped from existing research[16–19]. The theoretical conclusion would later be verified by results in software simulation and experiments in a real communication system in the laboratory. Finally, this article would present a record-breaking 31.38 Gb/s single-chip communication rate.

Device and modeling method

8-wavelength LED array device

In Figure 1(a), it demonstrates the layout of the LED array chip. Each color has a pair of LED units and the total array can emit light with eight different wavelengths: 450 nm, 480 nm, 500 nm, 520 nm, 550 nm, 570 nm, 620 nm, and 660 nm. The sizes of the units are mostly 27 mil (0.686 mm), but 520 nm (25 mil, 0.635 mm), 570 nm (45 mil, 1.143 mm), and 660 nm (42 mil, 1.067 mm) LED units are the exceptions. Compared with an earlier design[25], it reduces the LED size, which trades the optical output for communication performance. And its electrical circuit design allows each LED unit to be simultaneously driven as a WDM system that can parallelly and independently transmit data in at most 8 channels. Compared with a single-LED VLC system, this structure multiplies the channel capacity and is compatible with the trend for increasing the data rate of VLC systems.

The V-pit is a special structure in the GaN-based LED device. They are “V-shaped” pits on the active layer[26]. Fig. 1(b) shows the morphology of the active layer taken by scanning electron microscope (SEM). It demonstrates the hexagon edge of the V-pit. Each hexagon in this picture is about 0.2–0.4 μm in diameter, but its size and density are adjustable in the fabrication, for instance, by controlling the number of superlattice periods in the preparation layer[14]. Previous research has shown its importance in alleviating the “yellow gap” problem, which enables green and yellow GaN-based LED to work in practical wall plug efficiency[27] (33.7%, previous records are usually below 10%). Study on such mismatch has shown it could cause severe compressive strain and defects[28]. Meanwhile, the Indium segregation also causes the device to suffer from the quantum-confined Stark effect[29] (QCSE). V-pit alleviates the stress in QWs and also the QCSE, meanwhile creating a second channel for the carrier to enter the well, and by horizontal transportation,

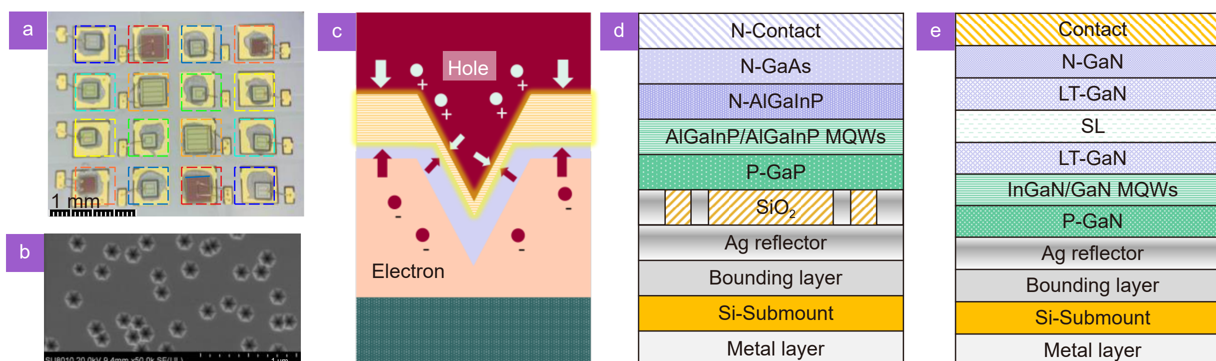

Fig. 1 | (**a**) The proposed 8-wavelength 4x4 LED array chip image, the colors of each dash line box represent the color of the LED unit. (**b**) The scanning electron microscope (SEM) image of the V-pit structure. (**c**) The vertical profile of the V-pit structure. (**d**) Layers of the red LED units (660 nm and 620 nm). (**e**) Layers of the GaN-based LED units (wavelengths from 570 nm to 450 nm).

they are injected into the flat wells[26].

The detailed profile of the V-pit is shown in Fig.1(c). The most prominent effect of the V-pit is that it allows the carriers to enter the quantum well from the sides of the pit. This area is named "sidewall quantum well", which creates a second branch for the current. Such quantum wells are featured in thinner width and therefore facilitate the carriers to enter the quantum well region. Afterward, those carriers are horizontally transported into the flat quantum well region to increase the carrier density, accelerating the recombination process, especially the radiative recombination. This innovation brings a marked improvement in illumination efficacy, particularly for LEDs in the long wavelength range, such as yellow and green. This will be further explored in the following part of this paper.

The detailed structures of LED units are plotted in Fig. 1(d) and 1(e). 620 nm and 660 nm LED units use AlGaInP material to fabricate the quantum well region. Their detailed structure is demonstrated in Fig. 1(d). The LED units whose wavelength are shorter than 570 nm (including 570 nm) are GaN-based LEDs grown on the C-plane, and their layer structure is illustrated in Fig. 1(e). Both LED units have an Ag reflector to reflects the backward emission and increase the external quantum efficiency (EQE). The reason for choosing a different material for red LEDs is that the electrical-optical performance of GaN-LED deteriorates as the emission wavelength moves longer, and at present, it is still challenging for GaN-LED to emit red light efficiently.

Software simulation to V-pit structure and sidewall quantum well

The first software simulation in Fig. 2 shows the influence introduced by V-pits on the carrier behavior in the active layers. The current density simulation result shows that the h+ (holes) have two routes to enter the quantum wells and the sidewall area attracts more carriers than the flat quantum wells. The arrows in Fig. 2(a) indicate the direction and strength of the local h+ (hole) current. It clearly shows that a strong current flows alongside the boundary of the flat well region and reaches the sidewall quantum well region. The positive carriers is concentrated in the V-pit later, and next move across the energy barriers of the sidewall quantum. Next, holes horizontally flow into the flat quantum well. The detailed view in Fig. 2(b) clearly shows that carriers enter the V-pit via several positions on the sidewall, where the current density here is remarkably stronger than the average value. This simulation reveals the connection between the V-pit structure and the carrier dynamics. Although V-pits do not occupy a large proportion of the active layer area, such a high current density suggests that it would create a new path for carriers that significantly changes the EO characteristics.

The second simulation in Fig. 3 compares the recombination rate of the two samples in the simulation. In communication, the high-frequency response is critical to achieve high modulation bandwidth, and it is closely related to the radiative recombination rate[30–32]. A higher recombination rate means a lower carrier lifetime and better high-frequency performance. Figure 3(a) and 3(b) present the highest recombination rate of all types (SRH, radiative, and Auger) inside each quantum well. In either 30 mA or 350 mA cases, the sample with a V-pit demonstrates a larger rate by orders of magnitude. Meanwhile, the rate among the five quantum wells does not show an exponential decrease as the quantum well position changes from the front (No. 1) to the rear side (No. 5). In comparison, the sample without a V-pit not only suffers

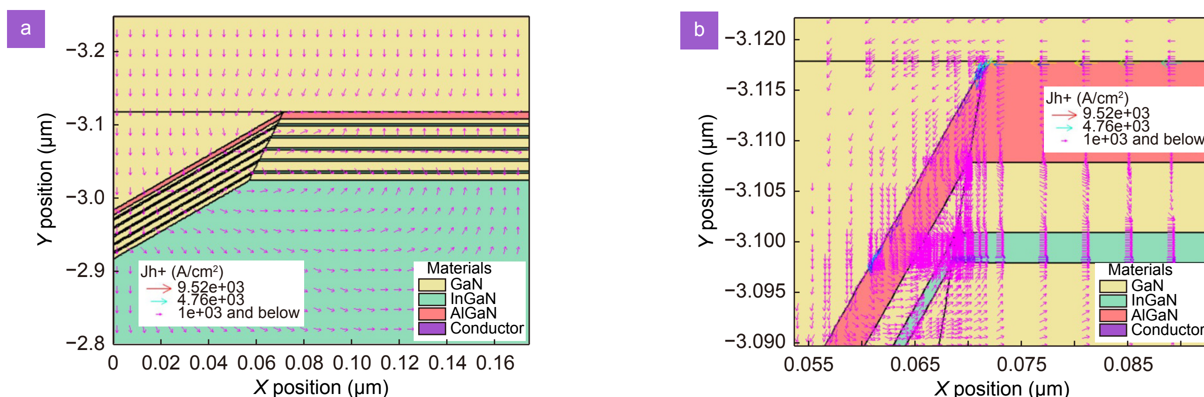

Fig. 2 | The current density distribution in simulation (**a**) and its detailed view (**b**). The h+ carriers are attracted by the V-pit structure and enter the sidewall quantum well area. Next, they are horizontally transported into the wells in the flat quantum wells and increases the injection into these wells.

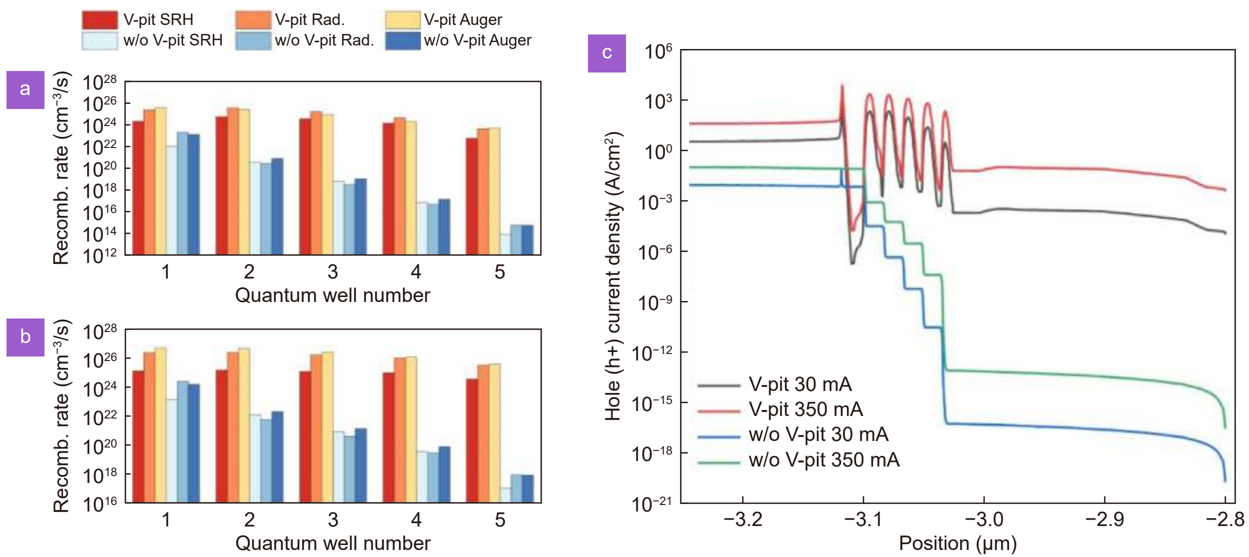

Fig. 3 | Comparison of the maximum recombination rate (SRH, Radiative, and Auger) between the sample with and without V-pits in each quantum well in 30 mA (**a**) and 350 mA (**b**) cases. (**c**) The hole current density simulation for samples with or without V-pits. Notice that the sample with V-pit presents a significant gain in current density in each quantum well.

from lower recombination rate, especially the radiative recombination but also a dramatic decrease versus the quantum well position.

The difference in recombination rate can be explained by the current density simulation results in Fig. 3(c). It selects the intersection X = 0.08 μm, and plots the current density along the Y position. It is the flat area for both samples with or without V-pit. As the holes move from the P side to the N side, the quantum wells closer to the P side gain the majority of holes. Apart from the consumption in recombination, the quantum barriers among the quantum wells also prevent the holes from entering the quantum wells near the N side. This causes an exponential decay in the current density in the sample without a V-pit. However, the V-pit sample is benefitted from the sidewall structure, which has a much thinner quantum barrier and thus allows the holes to enter the quantum wells near the N side, and next, be horizontally transported into the flat area. This difference in carrier dynamics causes a dramatic difference in the carrier density and significantly influences the recombination rate in Fig. 3(a) and 3(b). A higher carrier recombination rate suggests a shorter carrier lifetime and larger bandwidth. To validate the result from the software simulation, we build an equivalent circuit model according to the simulation and use the model to fit the measured S21 curves.

Equivalent circuit modeling

The equivalent circuit method has shown its effectiveness in relative research about LED modeling[19,33]. A previous study has shown a general method to fit the LED impedance and transfer characteristics[33]. It models the LED with three parts: the intrinsic LED structure; the bounding parasitic elements, and the ESD circuit. In the part representing the intrinsic LED, it uses a resistor for the serial resistance, a capacitor for the junction capacitance, and another resistor parallel to the capacitance to represent the dynamic resistance. It assumes a linear relationship between the power on the dynamic resistance and the received signal power and obtains an accurate fitting result to the measured S21 parameter. We modify and extend this model to suit the case in LED devices with V-pit in this paper.

The equivalent circuit demonstrated in Fig. 4(a) also includes 3 parts: the intrinsic LED part that represents the active layers, which mainly determines the performance of the LED device; the package and bounding part that resembles the bounding layers in the device and package in the system; the parasitic elements that represent the remaining error after calibration. Since the simulation process has demonstrated the significance of the current through V-pits. Different from the model mentioned in previous research[33], the circuit for the intrinsic LED part has two branches as if there are two LEDs. The V-pit structure creates a second path for the carriers to enter the quantum wells and it deserves a dedicated branch in the circuit. This idea also appears in a previous study[34] that treats the LED with V-pits as two parallel

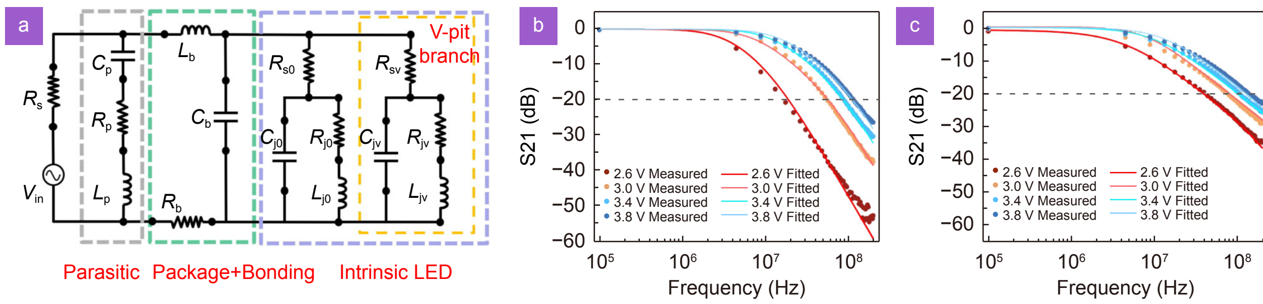

Fig. 4 | (**a**) The proposed equivalent circuit for fitting both LEDs with and without V-pits (with tiny V-pits). The branch in the dash yellow box is dedicated to representing the extra current introduced by the V-pit area. And the other branch in the intrinsic LED part represents the flat quantum well region. The fitting result using the proposed equivalent circuit for (**b**) the sample without V-pits and (**c**) the sample with V-pits.

LEDs. The parallel relationship between the two branches suggests an extra optical power as the total impedance is reduced and hence increases the current flows into the quantum well. Interestingly, this model also works for the LED sample because in practice there are inevitably tiny V-pits in the active layer even when measures are taken to eliminate such structure[35]. The size of V-pits would influence the model parameters. Meanwhile, this equivalent circuit introduces an inductor parallel to the dynamic resistance R_{j0} and R_{jv} to represent the inductance in the quantum wells, which helps the model to fit the high-frequency part of the S21 measurement.

By controlling the fabrication process, samples with or without V-pits (actually containing tiny V-pits) in the active layers are produced to validate the theoretical conclusion and simulation result. They are tested using a PD and network analyzer to obtain the transfer characteristic, and an Everfine HAAS-3000 spectroradiometer to acquire the illumination performance versus bias current. The S21 is measured using an E5071C network analyzer, Keysight. The LED samples are biased using ZFBT-4R2GW+ bias tee, Mini-Circuits. The signal is received using 818-BB-21A, Newport with a built-in 26 dB transimpedance amplifier (TIA). The passband of the bias tee is from 100 kHz to 4.2 GHz, and the PD rise time is less than 500 ps. To obtain the predicted S21 curves, we first use the model to fit the measured impedance using the genetic algorithm (GA), and next, we use the model to generate its theoretical S21.

The fitted S21 result is shown in Fig. 4(b) and 4(c). The S21 prediction and the data obtained from the experiment agree well. The sample with V-pit has a notably larger −20 dB bandwidth compared with the sample without V-pit. The standard deviation of the S21 curve is less than 3 dB. In the meantime, the difference in model parameters also agrees with the result in the simulation or already published studies. For example, the L_{j0} parameter tells that, with the help of V-pits, the inductance in the flat quantum wells region is dramatically reduced by an order of magnitude. It suggests that there is less impedance and larger optical power for high-frequency input signals. It agrees with the simulation result that the V-pit sample has a larger current flow and higher radiative recombination rate (also means shorter carrier lifetime and larger bandwidth). Meanwhile, the serial resistor R_{sv} for the sample with V-pits is below 100 Ω, but the sample without V-pits is 500–1500 Ω. This difference suggests that there are still tiny V-pits in such sample, and the result in an insignificant current path apart from the main one directly passing the flat quantum well region, which agrees with the SEM images shown in previous research[35].

Sample electric-optical performance comparison

The electrical-optical performance of the samples is also measured using the HAAS-3000 spectroradiometer from Everfine Company. Fundamental optical-electronic performance is plotted. Figure 5(a) compares the I-V curve between samples with or without V-pits. Firstly, the lower resistance means lower heat dissipation given the same bias current. Secondly, the lower resistance in the V-pit sample suggests a higher optical signal in the modulation process[30]. The same conclusion could be drawn from Fig. 5(b). The optical power of the V-pit sample outperforms the sample without V-pits by 20%–30% throughout the test. Compared with the sample without V-pits, V-pits increase the luminous efficacy by 88.6% and 50.35% in the smallest current density (1.91 A/cm^2) and the highest one (22.96 A/cm^2), respectively. Even though the droop effect appears in both devices and their luminous efficacy decreases by more than 50%, the sample with V-pits maintains its advantage in high

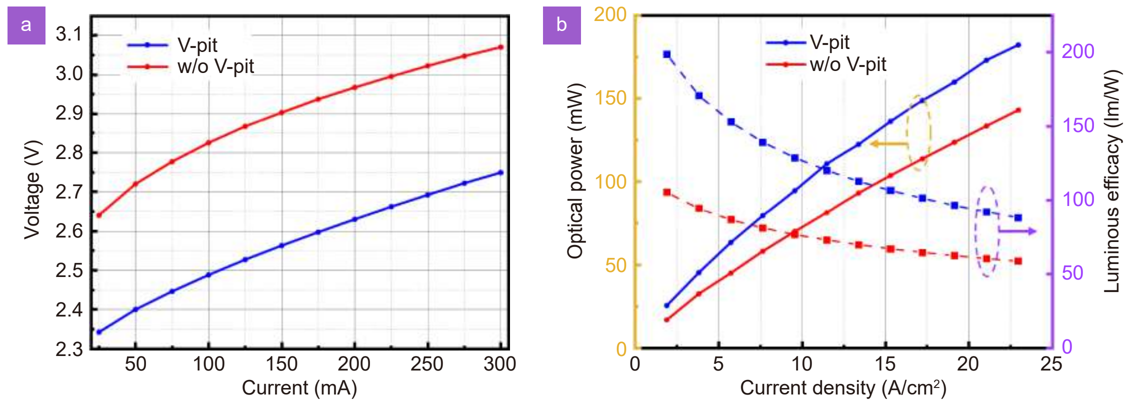

Fig. 5 | (**a**) The comparison between the I-V curves of the LED sample with or without the V-pit structure. (**b**) The LI (left *y*-axis) and illumination efficacy (right *y*-axis) versus the current density of the LED sample with or without the V-pit structure.

current density cases.

The emission spectrum is presented in Fig. 6. It compares the spectra in peak wavelength and the full-width-half-maximum (FWHM). The peak wavelengths of the two are approximately the same as their quantum well region adopts the same material and energy band design. They both demonstrate a "blue shift" phenomenon as the bias current increase from 25 mA to 400 mA, which is attributed to the distorted energy band in such a strong electric field. However, their FWHMs present a noticeable difference. Figure 6(c) records the change in FWMH versus the bias current. Although both lines show a growing trend, the sample with V-pits has a smaller FWHM. The difference in FWHM at 25 mA is the largest (18%), and it gradually decreases as the bias current increases. At 300 mA, the gap is narrowed to 12%. The reason is that in a higher bias current, the carrier recombination would include more various energy levels and spread the energy distribution onto the emission spectrum. It would impact both samples and reduce the advantage of the V-pit sample. Smaller FWHM means a more concentrated emission on the spectrum, and the optical power loss caused by optical filters for WDM systems in practice would be smaller.

To compare the time-domain transient response of the samples, they are tested in a communication system with the same pre-equalization that compensates for the high-frequency loss. Figure 7 shows their pulse response in the time domain to a 1 GHz bandwidth sinc function input. Both devices demonstrate a narrower pulse when the bias current increases from 60 mA to 300 mA. But the V-pit sample has a better impulse response than the other one, especially in the low bias current region. In the 60 mA bias current case, the sample without V-pits takes 6 ns to return to 1/e of the peak level, but V-pits reduce this value to about 1.6 ns. Meanwhile, when the Vpp is set high (the second row), the nonlinearity problem appears, and it notably distorted the pulse. The responses for both samples are spread wider, and the sample without V-pit even demonstrates a "plateau" in the

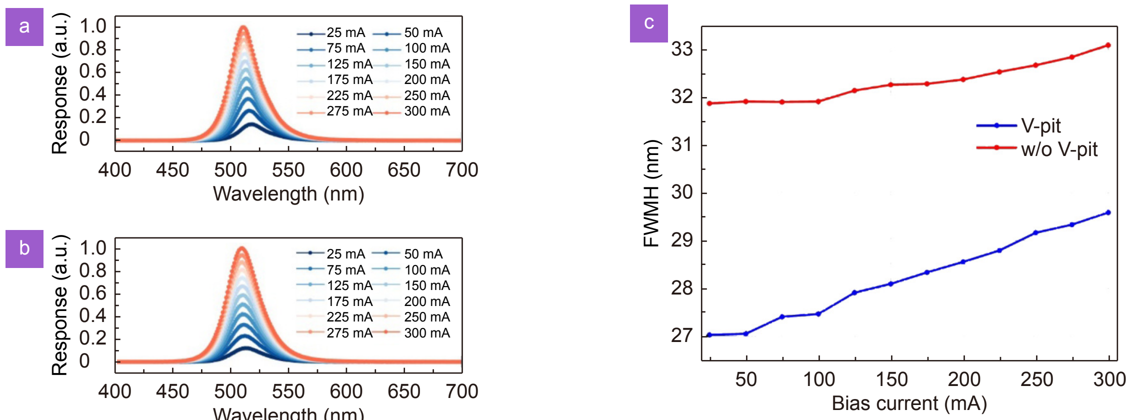

Fig. 6 | (**a**, **b**) The electroluminescence (EL) spectrum of the LED samples with and without V-pits. (**c**) The full-width-half-maximum (FWHM) of EL spectrum shown in (a) and (b).

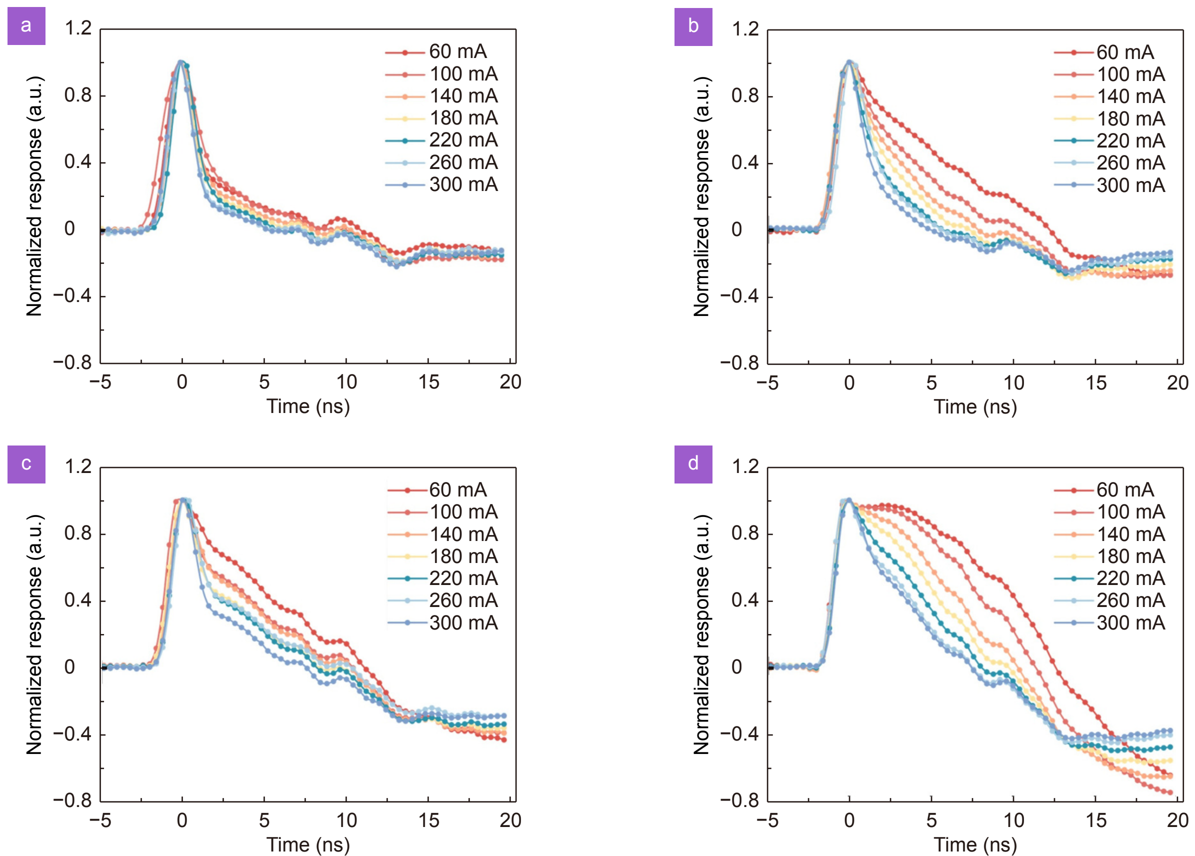

Fig. 7 | (**a**, **b**) The pulse response of the LED samples with and without V-pits in 300 mV Vpp. (**c**, **d**) The pulse response of LED samples with and without V-pits in 1 V Vpp.

highest part of the response curve. But the V-pit sample is less influenced by the nonlinearity and maintains a narrower response. In summary, the sample with V-pit owns a significantly narrower pulse width. Even in strong nonlinearity, the pulse width is not remarkably larger than the sample without V-pits in small Vpp. The shorter "tail" of the pulse response represents a weaker dispersion in the time domain and causes less inter-symbol interference (ISI) because there would be less overlap between adjacent symbols. The results support the prediction made from the device recombination simulation, that a faster carrier transportation results in a faster response to the input electrical signal.

Communication experiment setup

The communication system setup is shown in Fig. 8. The arbitrary waveform generator (AWG) is AWG710, Tektronix. The OSC is MSO9404A mixed signal oscilloscope, Agilent Technologies. The electrical amplifier (EA) is ZHL-2-8-S+, Mini-Circuits. The bias tee is ZF-BT-4R2GW-FT+, Mini-Circuits. The photodetector (PD) is Hamamatsu S10784 equipped with a TIA mounted on a homemade PCB board. The TIA generates two outputs to the OSC to calculate the differential signal for the RX DSP process. There are two stages in the communication process: the channel estimation stage and the communication stage.

In the channel estimation stage, the original bits skip the bit-power loading process and are modulated using QAM (usually QPSK in this stage). Later DMT is applied to convert the symbols into time domain waveform. Before sending into the AWG, the modulated waveform needs a digital pre-equalization (DZN) to enhance the high-frequency part and achieve a flatter spectrum at the receiver side. It resembles the function of a hardware pre-equalizer but processes the signal in the digital domain.

The optical path is illustrated on the left side of Fig. 8. The signal from the AWG is firstly amplified by an electrical amplifier, and later coupled with a DC bias current to drive the LED. The emitted optical signal passes through a lens system (two lenses at TX and one at RX) to reach the PD. To control the signal power and prevent the PD from saturation, an aperture is added to the

path before the PD. To select a specific wavelength channel, an optical filter could be placed at RX, but to reduce the complexity in the optical path setup, this experiment chose to omit this element and lit different LED units in turn. The electrical signal produced by PD is amplified by a differential TIA. The output ports are connected to an oscilloscope (OSC) for recording.

The recorded waveform later experiences synchronization, TL-BiGRU nonlinear post-equalization (a bi-directional GRU network using transfer learning technique to reduce computation complexity), and DMT demodulation to recover the original data before DMT modulation, which has been proven effective to mitigate the nonlinearity in our previous study[15]. By estimating the signal-to-noise ratio (SNR) at each subcarrier, a more efficient bit allocation plan is obtained. Next in the communication stage, this solution is used to modify the modulation order upon each subcarrier. The rest of the process is the same as the channel estimation stage. When the final output bits achieve the desired forward-error-correction (FEC) bit error rate (BER) threshold (0.0038 for 7% hard-decision FEC), the data rate could be acknowledged as a feasible communication rate. Otherwise, the transmission rate is lowered by tuning the sample rate of AWG until the BER satisfies the requirement.

Results and discussion

To achieve the best communication process, we measured the estimated spectrum efficiency (SE) using the channel estimation function of the communication system. But it skips the nonlinear post-equalization process to output the rough estimation to the channel. The best working points are estimated from the contour diagrams in Fig. 9. The best working points are distributed within 100–280 mA bias current and 300–700 mV Vpp. The working points suggest that the optical output is sufficient when the units perform their best. In the communication experiment, the actual Vpp could be approximately 50 mV higher than the best working point in the estimation as the nonlinearity in the channel is effectively mitigated by the TL-BiGRU algorithm but signal power and SNR are improved.

The signal spectra of each channel are shown in Fig. 10. There is about −30 dB loss at the high-frequency end of the band compared with the low-frequency part before applying Bi-GRU. But Bi-GRU successfully recovers the amplitude in the middle and high-frequency spectra and alleviates the impairment due to the high-frequency loss. However, the impairment caused by noise could not be recovered, which could be identified from the spikes and minor fluctuation in amplitude within the modulation bandwidth. The modulation bandwidths of all the channels are also shown nearby each subplots in Fig. 10. The largest bandwidth is 800 MHz for 520 nm and 660 nm LED units. They are 23% larger than the lowest bandwidths of 550 nm and 570 nm. Compared with the previous V-pit device, the modulation bandwidth of 520 nm unit increases by 33%. The advantage in modulation bandwidth indicates a less severe loss in signal power,

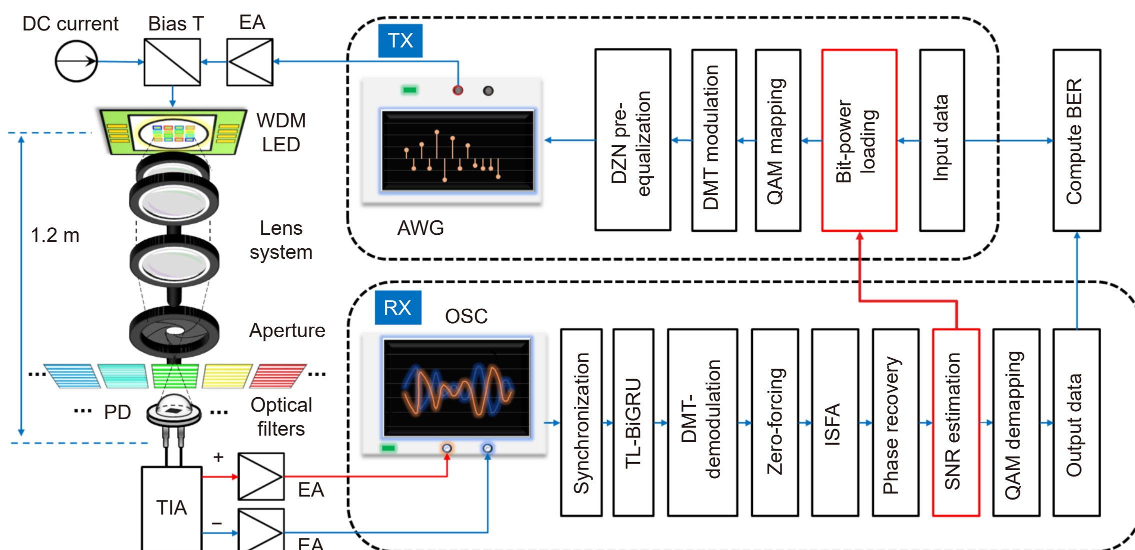

Fig. 8 | The setup diagram and the DSP process in the TX and RX sides. The red blocks represent the bit-power loading process which modifies the modulation order and power of each DMT sub-carrier and helps the system achieve higher spectrum efficiency and communication capacity.

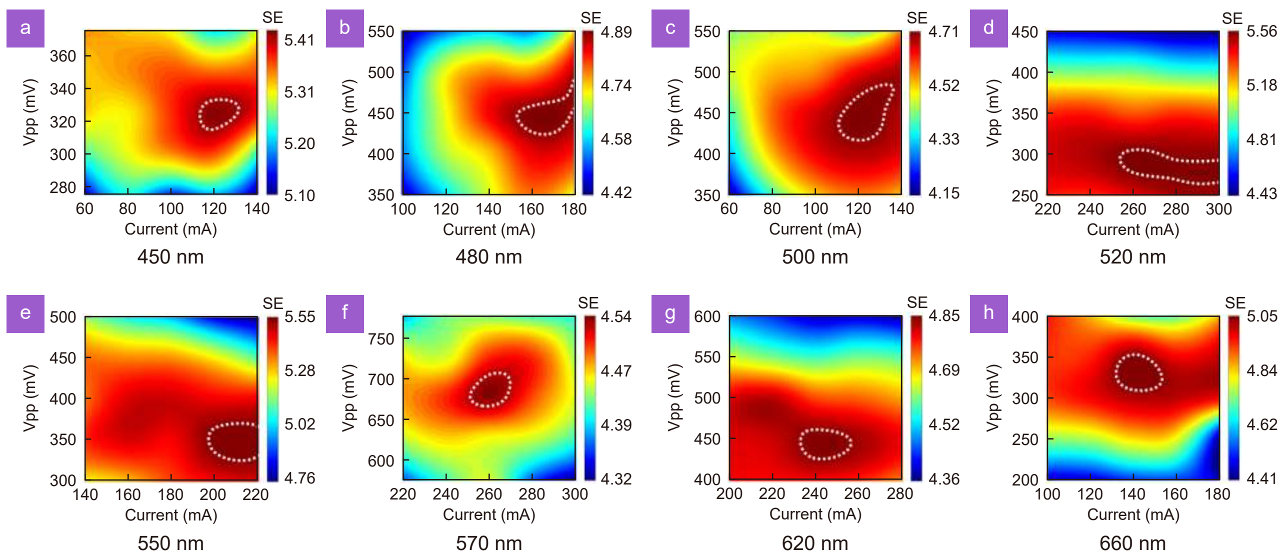

Fig. 9 | The contour diagrams of each LED unit in searching for the best working point of each channel.

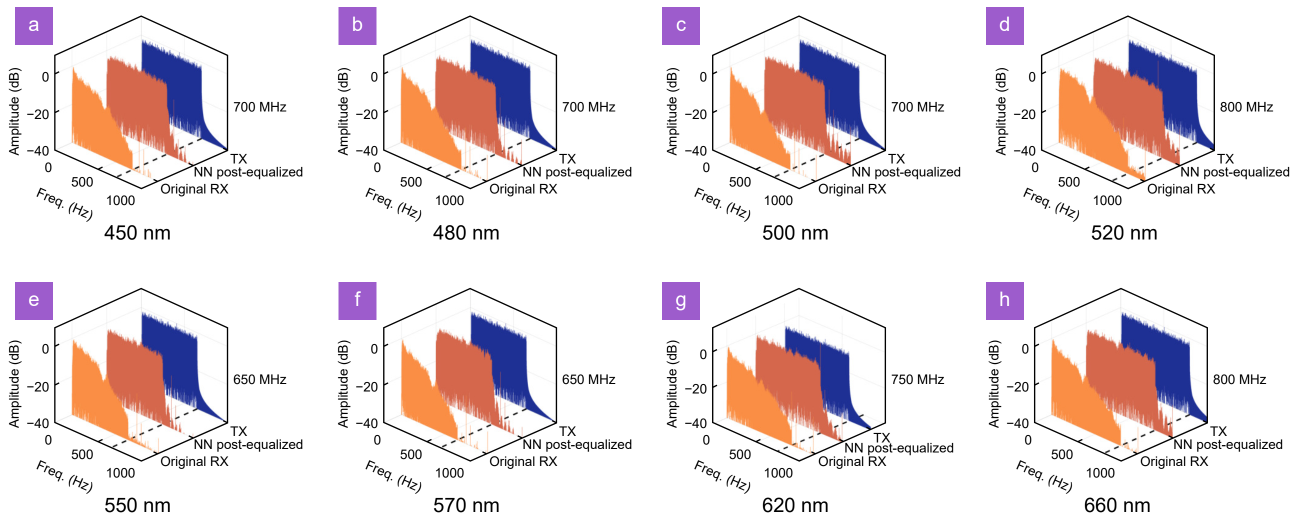

Fig. 10 | The spectra of the original, received and NN equalized signals in the channel estimation stage of the communication experiment for each channel.

especially in the high-frequency part of the spectrum.

The actual bit-power loading results are shown in Fig. 11 in the first row of each subplot. It shows the channel capacity of each subcarrier in DMT modulation and the adjustment to the power allocated to them according to the channel SNR estimation. The SNR levels in each channel could exceed 24 dB, allowing 128 QAM or even higher order to be modulated on this subcarrier. The highest SNR appears is 27.89 dB in the 143rd subcarrier in the 520 nm channel, and consequently, 256 QAM symbols are modulated onto this subcarrier. However, the modulation orders are low on both the lowest and highest sides of the spectrum due to the high noise level near DC and the high signal power loss in the high-frequency part of the spectrum. In the same channel, the 1st subcarrier only has 9.2 dB SNR and the SNR for the 498th is 12.0 dB.

Figure 11 also demonstrates the power ratio in the second row of each subplot. It is the ratio of the power allocated on each subcarrier after and before modification. It mainly varies from 0.8 to 1.2. A ratio larger than one means the carriers that receive enhancement from those whose power ratio is smaller than one. If the power level on a specific subcarrier is adequate, the excessive power would be allocated to other subcarriers that require a lift in power to reach a higher modulation order. The subcarrier that requires the least amount of enhancement in power has the highest priority for power redistribution. A general trend among the 8 diagrams in Fig. 11 is that the subcarriers located between No.100 to 200 often exhibit a sufficient SNR for the designated modulation order. They usually transfer their excessive

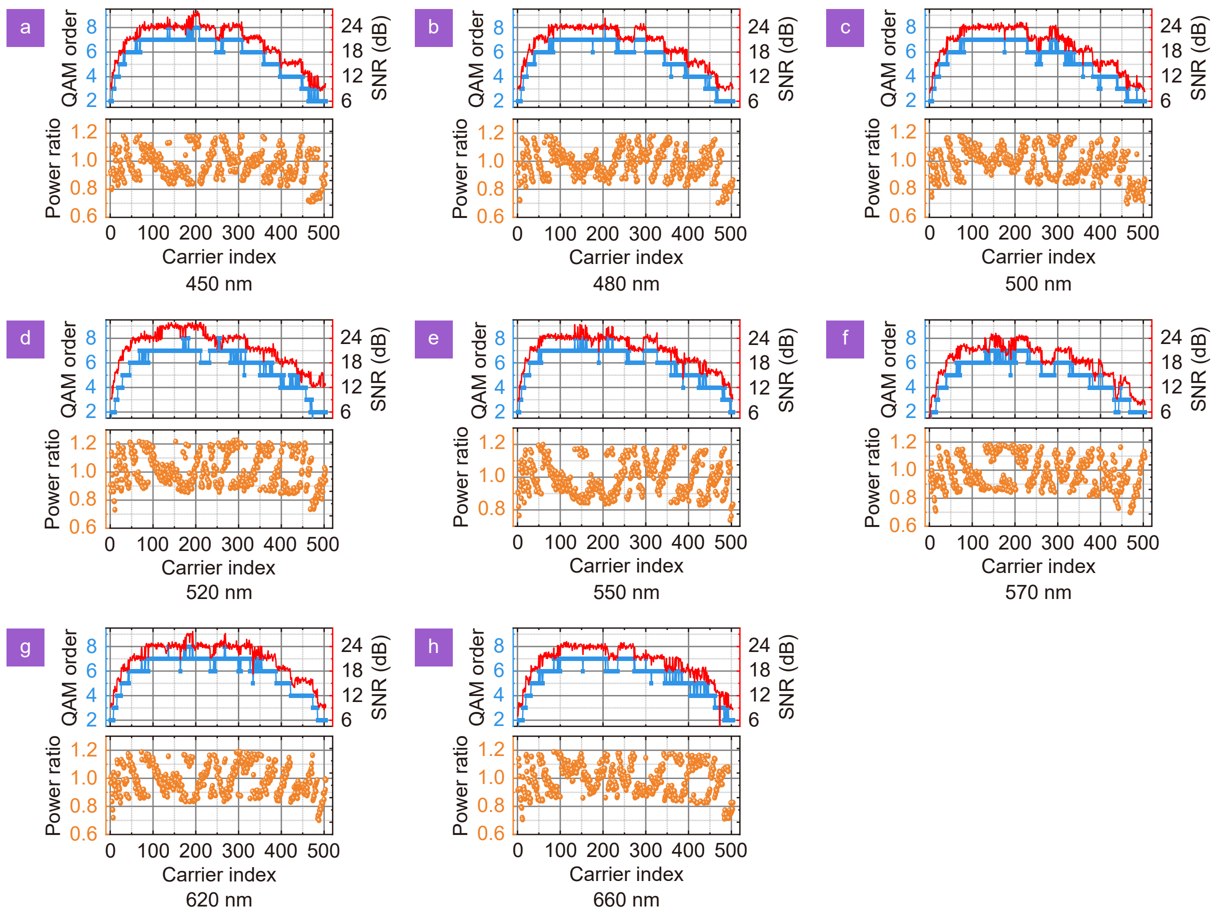

Fig. 11 | The bit-power loading result in the final communication test. The first row of each subplot shows the modulation order and SNR on each subcarrier, and the second row is the allocated power ratio, demonstrating the modification to the power of subcarriers.

power to other subcarriers located near sudden changes in SNR, where some subcarriers require a small amount of power to support higher modulation orders. As a result, the modified power allocation more efficiently utilizes the available signal power, and the final data rate increases without increasing the total signal power.

The spectrum efficiency and bandwidth applied for each channel are listed in Fig. 12(a). The spectrum efficiency for all the LED units ranges from 4.97 to 5.91, showing that the LED array can provide a large optical output and SNR that is sufficient for a high data rate. The red 660 nm LED unit with AlGaInP QW layer and 520 nm GaN-based LED has the largest channel bandwidth (800 MHz), followed by the 620 nm LED unit and the short wavelength GaN-based LED from 450 nm to 520 nm. The smallest bandwidth is 650 MHz for the 550 nm and 570 nm GaN-based LED units. The yellow spectrum longer than 570 nm is a long wavelength that requires higher Indium composition in the quantum well and hence deteriorates the quality of the wells in large bias current. Even though V-pits provide an enhancement to its performance GaN-based LED still suffers from lower efficiency compared with LED units, which causes the lowest data rate in the 570 nm channel. All of the rates are achieved under the BER threshold 0.0038 in Fig. 12(b). By applying 7% HD-FEC the error bits could be corrected and error-free (BER<10^{-9}) transmission would be secured after the decoding process.

The final communication performance is summarized in Fig. 12(c). The total data rate of the LED array is 31.38 Gb/s. It is 29.4% larger than the result in the earlier study[25] in 2021. Compared with the original design, the largest three improvements in both data rate and percentage belong to the long-wavelength GaN-based LED. In the 520 nm channel, the record in 2021 is 2.80 Gb/s, but it significantly increased by 57.20% (1.60 Gb/s) in this experiment. The data rate in 550 nm and 570 nm wavelength channels improves by 48.9% (1.24 Gb/s) and 40.0% (0.91 Gb/s), respectively. The improvements in red LED units are less significant. The 620 nm LED data rate increases by 26.5% (900 Mb/s). And the 660 nm LED data rate is improved by 25.6% (890 Mb/s). The blue LED exhibits the least incremental advancement: the 450 nm, 480 nm, and 500 nm LEDs only achieve

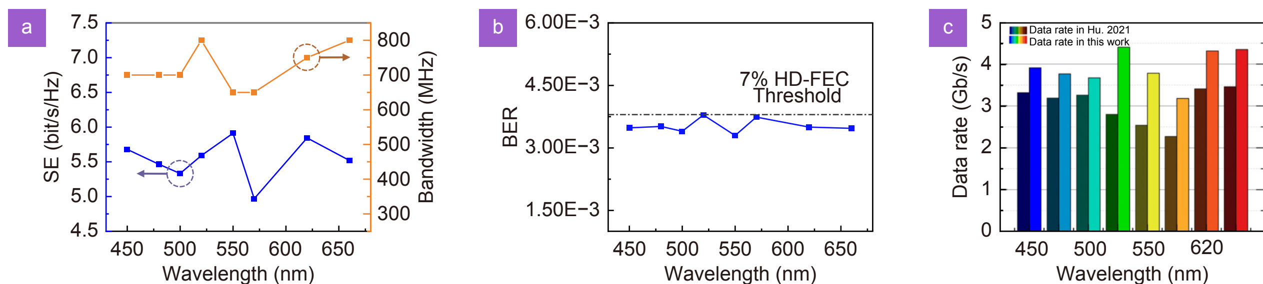

Fig. 12 | Summary of the communication rate. (**a**) The spectrum efficiency (SE) and modulation bandwidth of the proposed 8-wavelength WDM system. (**b**) The BER of each channel, all the BERs are lower than the 7% HD-FEC threshold. (**c**) Comparison in data rate with the original design. The total data rate of the proposed size-improved design device is 31.38 Gb/s.

17.86% (590 Mb/s), 18.03% (580 Mb/s), and 12.69% (410 Mb/s) increase in data rates compared with the original design. It deserves attention that although the PD is more sensitive to red than green spectrum. However, but the 520 nm GaN-based LED unit outperforms the LED 660 nm AlGaInP one in data rate. It means that the data rate of long-wavelength GaN-based LEDs in conventional "yellow gap" regions can also catch up with or even surpass their counterparts in other spectra, with the help of optimized V-pit design. This breakthrough significantly enhances the weakness of the GaN-based multi-color LED VLC system and plays an important role in the 7.13 Gb/s increase in total data rate.

Conclusions

In this work, we investigate the function of the V-pit structure and demonstrate its merits in high-speed VLC applications. Due to the advantages in optimized device design and DSP, the channel capacities of the proposed GaN-based LED array device from short wavelength channel to high wavelength ones are 3.91 Gb/s, 3.77 Gb/s, 3.67 Gb/s, 4.40 Gb/s, 3.78 Gb/s, 3.18 Gb/s, 4.31 Gb/s, and 4.35 Gb/s. The total rate of the system is impressively 31.38 Gb/s, exceeding its earliest design in 2021 by 29.38%. The large channel capacity suggests that a multi-color V-pit enhanced GaN-based LED array is a promising technology in the upcoming 6G era. The equivalent circuit model and simulation suggest that V-pits significantly enhance the device performance by introducing a second current branch, which not only improves its fundamental EO characteristics but also enhances its response to high-frequency signals and the modulation bandwidth in the communication system. The device improvement in the green and yellow spectrum is the most prominent. In earlier experiments, the 520 nm green light LED unit is outperformed by the best AlGaInP LED in a 660 nm channel. However, in this experiment, it gains a notable enhancement that makes its data rate exceed the best AlGaInP LED unit by reducing size dimension. Meanwhile, 550 nm and 570 nm LED units also achieve remarkable improvement in data rate and percentage compared with the original design. It means that the "yellow gap" problem in communication can also be effectively handled by the V-pit structure, resulting in a competitive communication rate in the green and yellow wavelength. In future works, a more accurate and explainable modeling method deserves investigation to provide theories for improving the V-pit enhanced GaN-based LED and further increasing the channel capacity to satisfy the ultra-high communication capacity requirement of future wireless communication networks.

References

1. Juntti M, Kantola R, Kyösti P, LaValle S, De Lima C M et al. *Key drivers and research challenges for 6g ubiquitous wireless intelligence*. (2019).
2. Chen YW, Zhang R, Hsu CW, Chang GK. Key enabling technologies for the post-5G era: fully adaptive, all-spectra coordinated radio access network with function decoupling. *IEEE Commun Mag* **58**, 60–66 (2020).
3. Giordani M, Polese M, Mezzavilla M, Rangan S, Zorzi M. Toward 6G networks: use cases and technologies. *IEEE Commun Mag* **58**, 55–61 (2020).
4. Chi N, Zhou YJ, Wei YR, Hu FC. Visible light communication in 6G: advances, challenges, and prospects. *IEEE Veh Technol Mag* **15**, 93–102 (2020).
5. Sharma H, Jha RK. VLC enabled hybrid wireless network for B5G/6G communications. *Wireless Pers Commun* **124**, 1741–1771 (2022).
6. Wei ZX, Wang ZM, Zhang JA, Li Q, Zhang JP et al. Evolution of optical wireless communication for B5G/6G. *Progress Quantum Electron* **83**, 100398 (2022).
7. Qiu PJ, Zhu SJ, Jin ZX, Zhou XL, Cui XG et al. Beyond 25 Gbps optical wireless communication using wavelength division multiplexed LEDs and micro-LEDs. *Opt Lett* **47**, 317–320 (2022).
8. Hu FC, Holguin-Lerma JA, Mao Y, Zou P, Shen C et al. Demonstration of a low-complexity memory-polynomial-aided neural network equalizer for CAP visible-light communication with superluminescent diode. *Opto-Electron Adv* **3**, 200009 (2020).
9. Chang YH, Huang YM, Gunawan WH, Chang GH, Liou FJ et al. 4.343-gbit/s green semipolar (20-21) μ-LED for high speed vis-

ible light communication. *IEEE Photonics J* **13**, 7300204 (2021).
10. Xu FF, Jin ZX, Tao T, Tian PF, Wang GB et al. C-plane blue micro-LED with 1.53 GHz bandwidth for high-speed visible light communication. *IEEE Electron Device Lett* **43**, 910–913 (2022).
11. Wang L, Wei ZX, Chen CJ, Wang L, Fu HY et al. 1.3 GHz E-O bandwidth GaN-based micro-LED for multi-gigabit visible light communication. *Photonics Res* **9**, 792–802 (2021).
12. Wei ZX, Liu ZX, Liu X, Wang L, Wang L et al. 8.75 Gbps visible light communication link using an artificial neural network equalizer and a single-pixel blue micro-LED. *Opt Lett* **46**, 4670–4673 (2021).
13. Lu TW, Lin XS, Guo QA, Tu CC, Liu SB et al. High-speed visible light communication based on micro-LED: A technology with wide applications in next generation communication. *Opto-Electron Sci* **1**, 220020 (2022).
14. Hu FC, Chen SQ, Zhang YY, Li GQ, Zou P et al. High-speed visible light communication systems based on Si-substrate LEDs with multiple superlattice interlayers. *PhotoniX* **2**, 16 (2021).
15. Niu WQ, Xu ZY, Liu Y, Lin XH, Cai JF et al. Key technologies for high-speed Si-substrate LED based visible light communicatioN. *J Lightwave Technol* **41**, 3316–3331 (2023).
16. Lin RL, Chen YF. Equivalent circuit model of light-emitting-diode for system analyses of lighting drivers. In *2009 IEEE Industry Applications Society Annual Meeting* 1–5 (IEEE, 2009); http://doi.org/10.1109/IAS.2009.5324876.
17. Deng W, Jin XC, Lv Y, Zhang XJ, Zhang XH et al. 2D ruddlesden–popper perovskite nanoplate based deep-blue light-emitting diodes for light communication. *Adv Funct Mater* **29**, 1903861 (2019).
18. Baureis P. Compact modeling of electrical, thermal and optical LED behavior. In *Proceedings of 35th European Solid-State Device Research Conference, 2005. ESSDERC 2005* 145–148 (IEEE, 2005); http://doi.org/10.1109/ESSDER.2005.1546606.
19. Han DP, Shim JI, Shin DS. Analysis of carrier recombination dynamics in InGaN-based light-emitting diodes by differential carrier lifetime measurement. *Appl Phys Express* **10**, 052101 (2017).
20. Niu WQ, Xu ZY, Xiao WH, Liu Y, Hu FC et al. Phosphor-free golden light LED array for 5.4-Gbps visible light communication using MIMO tomlinson-harashima precoding. *J Lightwave Technol* **40**, 5031–5040 (2022).
21. Lin RZ, Jin ZX, Qiu PJ, Liao Y, Hoo J et al. High bandwidth series-biased green micro-LED array toward 6 Gbps visible light communication. *Opt Lett* **47**, 3343–3346 (2022).
22. Wei ZX, Wang L, Liu ZX, Zhang C, Chen CJ et al. Multigigabit visible light communication based on high-bandwidth InGaN quantum dot green micro-LED. *ACS Photonics* **9**, 2354–2366 (2022).
23. Chang YH, Huang YM, Liou FJ, Chow CW, Liu Y et al. 2.805 Gbit/s high-bandwidth phosphor white light visible light communication utilizing an InGaN/GaN semipolar blue micro-LED. *Opt Express* **30**, 16938–16946 (2022).
24. Ferreira RXG, Xie EY, McKendry JJD, Rajbhandari S, Chun H et al. High bandwidth GaN-based micro-LEDs for multi-Gb/s visible light communications. *IEEE Photonics Technol Lett* **28**, 2023–2026 (2016).
25. Hu FC, Chen SQ, Li GQ, Zou P, Zhang JW et al. Si-substrate LEDs with multiple superlattice interlayers for beyond 24 Gbps visible light communication. *Photonics Res* **9**, 1581–1591 (2021).
26. Quan ZJ, Wang L, Zheng CD, Liu JL, Jiang FY. Roles of V-shaped pits on the improvement of quantum efficiency in InGaN/GaN multiple quantum well light-emitting diodes. *J Appl Phys* **116**, 183107 (2014).
27. Jiang FY, Zhang JL, Xu LQ, Ding J, Wang GX et al. Efficient InGaN-based yellow-light-emitting diodes. *Photonics Res* **7**, 144–148 (2019).
28. Damilano B, Gil B. Yellow–red emission from (Ga, In)N heterostructures. *J Phys D:Appl Phys* **48**, 403001 (2015).
29. Yang XD, Zhang JL, Wang XL, Zheng CD, Quan ZJ et al. Enhance the efficiency of green-yellow LED by optimizing the growth condition of preparation layer. *Superlattices Microstruct* **141**, 106459 (2020).
30. Linnartz JPMG, Deng X, Alexeev A, van Voorthuisen P. An LED communication model based on carrier recombination in the quantum well. In *2021 IEEE 32nd Annual International Symposium on Personal, Indoor and Mobile Radio Communications (PIMRC)* 1–6 (IEEE, 2021); http://doi.org/10.1109/PIMRC50174.2021.9569261.
31. Shi JY, Xiao WH, Ha Y, Niu WQ, Xu ZY et al. 3.76-Gbps yellow-light visible light communication system over 1.2 m free space transmission utilizing a Si-substrate LED and a cascaded pre-equalizer network. *Opt Express* **30**, 33337–33352 (2022).
32. Zhao LX, Zhu SC, Wu CH, Yang C, Yu ZG et al. GaN-based LEDs for light communication. *Sci China Phys, Mech Astron* **59**, 107301 (2016).
33. Li XC, Ghassemlooy Z, Zvanovec S, Alves LN. An equivalent circuit model of a commercial LED with an ESD protection component for VLC. *IEEE Photonics Technol Lett* **33**, 777–779 (2021).
34. Wu XM. Study on the luminescence properties of V-pit-containing GaN based blue LEDs on Si substrates (Nanchang University, Nanchang, 2014).
35. Gao JD, Zhang JL, Quan ZJ, Pan S, Liu JL et al. Effect of horizontal *p*–*n* junction on optoelectronics characteristics in InGaN-based light-emitting diodes with V-shaped pits. *J Phys D:Appl Phys* **53**, 335103 (2020).

Acknowledgements

This research was funded by the National Key Research and Development Program of China (2022YFB2802803), the Natural Science Foundation of China Project (No. 61925104, No. 62031011, No. 62201157, No. 62074072).

Author contributions

Z. Y. Xu, W. Q. Niu, and N. Chi proposes the main idea and supervised the project. F. Y. Jiang, J. L. Zhang, X. L. Wang, G. X. Wang, and L. Yu, design and fabricate the samples for experiment or complete the software simulation. Z. Y. Xu, W. Q. Niu, X. H. Lin, J. F. Cai, and J. Y. Shi participate in the DSP algorithm design. Z. Y. Xu writes the original draft. S. H. Yu, Z. X. He, N. Chi, C. Shen, and J. W. Zhang give feedback on editing this draft.

Competing interests

The authors declare no competing financial interests.

Supplementary information

Supplementary information for this paper is available at https://doi.org/10.29026/oes.2023.230005